Particle dynamics in asymmetry-induced transport

D. L. Eggleston
Occidental College, Physics Department, Los Angeles, California 90041

(Received 6 November 2006; accepted 29 November 2006; published online 12 January 2007)

The particle dynamics of asymmetry-induced transport are studied using a single-particle computer simulation. For the case of a helical asymmetry with axial and azimuthal wavenumbers (k,l) and with periodic boundary conditions, behaviors consistent with analytical theory are observed. For the typical experimental case of a standing wave asymmetry, the code reveals dynamical behaviors not included in the analytical theory of this transport. The resonances associated with the two constituent helical waves typically overlap and produce a region of stochastic motion. In addition, particles near the radius where the asymmetry frequency ω matches l times the $E\times B$ rotation frequency ω_R can be trapped in the potential of the applied asymmetry and confined to one end of the device. Both behaviors are associated with large radial excursions and mainly affect particles with low velocities, i.e., $v_z<2\omega_T/k$, where ω_T is the trapping frequency. For the case of a helical asymmetry with specularly reflecting boundaries, large radial excursions are observed for all velocities near the radius, where $\omega=l\omega_R$. Minor modifications to these results are observed when the code is run with realistic end potentials. © *2007 American Institute of Physics*.
[DOI: 10.1063/1.2424431]

I. INTRODUCTION

The Malmberg-Penning non-neutral plasma trap is especially suitable for basic studies of plasma transport due to its excellent confinement properties. It is well established that electric and magnetic fields that break the cylindrical symmetry of these traps produce radial transport. This asymmetry-induced transport has been studied experimentally for some time, both for its fundamental interest and because suitably applied asymmetries can drive particles radially inward and produce essentially infinite confinement times for various applications.[1–9] While it is straightforward to observe this transport in experiments, a full understanding of the transport remains elusive. Calculations of the local particle flux $\Gamma(r)$ produced by the field asymmetry have been published for both the quasilinear (plateau) regime[10,11] and the nonlinear (banana) regime,[10] but a detailed comparison of some of the predictions of these theories with experiment[7] shows serious discrepancies. It seems clear that some important physics is missing from the theory.

In this paper we report results from a simple computer simulation developed as an aid to understanding particle dynamics in asymmetry-induced transport. The code employs the fourth-order Runge-Kutta method to advance single particles in prescribed fields matching our experiment. For a single helical asymmetry with periodic boundary conditions, significant motion in the radial direction is restricted to those particles near the resonant velocity. Both the location and the width of this resonance are consistent with analytical theory. When a standing wave asymmetry is used, however, additional dynamical behaviors are observed not included in the current theory. Stochastic motion occurs when the resonant regions of the two constituent counterpropagating helical waves overlap, allowing a larger population of particles to undergo large radial excursions. This case also produces a class of particles with restricted axial motion in the lab frame. We also report additional dynamical behaviors for the case of a single helical asymmetry with reflecting boundary conditions. Finally, we investigate the effect of more realistic boundaries at the ends of the device and find minor modifications result.

II. MODEL

Our code is constructed to model our experimental device which is shown in Fig. 1. Low density electrons are confined in the central region of length L between the negatively biased injection gate and dump gate. In order to maintain an azimuthal $E\times B$ drift comparable to a higher density plasma, a negatively biased wire is stretched along the axis of the device. The uniform axial magnetic field B providing radial confinement is strong enough so that the gyroradius is much smaller than the wall radius R. The walls of the confinement region are divided into forty sectors (five axial divisions S1–S5 with eight azimuthal divisions each), which allow application of an asymmetric electric field. The voltages applied to these sectors are typically chosen so that the field consists primarily of a single Fourier mode. The remaining details of the experiment are given elsewhere.[7]

The code follows the dynamics of single particles in prescribed fields; interparticle fields are not included. The prescribed fields are set by the center wire potential, the asymmetric potential, and, when desired, the end confinement potentials. The center wire potential is given by

$$\phi_0(r) = \phi_{\mathrm{cw}}\frac{\ln(R/r)}{\ln(R/a)}, \tag{1}$$

where ϕ_{cw} is the bias of the center wire, R is the radius of the wall, and a is the radius of the center wire. The asymmetric potential is chosen to be either a helical wave

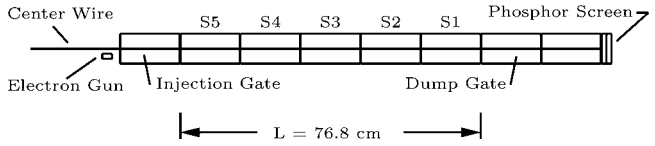

FIG. 1. Schematic of the Occidental College Trap. The usual plasma column is replaced by a biased wire to produce the basic dynamical motions in low density electrons injected from an off-axis gun.

$$\phi_{\text{asym}}(r,\theta,z,t) = \phi_1(r)\cos(kz - l\theta + \omega t) \tag{2}$$

or an axially standing wave

$$\phi_{\text{asym}}(r,\theta,z,t) = \phi_1(r)\cos(kz)\cos(-l\theta + \omega t). \tag{3}$$

In Eqs. (2) and (3), $k=n\pi/L$ and n is the axial wavenumber, l is the azimuthal wavenumber, ω is the asymmetry frequency, and z is measured from one end of the confinement region. The amplitude $\phi_1(r)$ is taken to be of the form $\phi_{10}(r/R)^l$, where ϕ_{10} is a constant. This form closely approximates the exact vacuum solution.

The particle motions in the code are governed by

$$\frac{dr}{dt} = v_r, \quad r\frac{d\theta}{dt} = v_\theta, \quad \frac{dz}{dt} = v_z, \quad \frac{dv_z}{dt} = \frac{qE_z}{m}. \tag{4}$$

For typical experimental conditions, the gyroradius is much smaller than the wall radius R and the cyclotron frequency is much larger that all other dynamical frequencies. We thus ignore the cyclotron motion and follow the motion of the guiding center. In this drift approximation, v_r and v_θ are given by

$$v_r = \frac{E_\theta}{B}, \quad v_\theta = -\frac{E_r}{B}. \tag{5}$$

The electric fields are obtained from the prescribed potentials: $E_r=-\partial\phi/\partial r$, $E_\theta=-(1/r)(\partial\phi/\partial\theta)$, and $E_z=-\partial\phi/\partial z$.

The code incorporates three options for the ends of the trap: periodic boundaries, specular reflection, or realistic ends. For periodic boundaries, the axial position of the particle can range from $z=-L$ to $z=L$. Particles reaching $z=L$ are shifted to $z=-L$ and vice versa. For specular reflection, the axial position ranges from $z=0$ to $z=L$. At the ends, the particle simply reverses axial direction as if bouncing off of an infinite potential. For realistic boundaries, the actual potentials produced by the negatively biased gates are added to the prescribed fields. In this case, the axial extent of the particle's motion is a function of radius and particle energy, and the azimuthal $E\times B$ rotation frequency ω_R is a function of r and z.

Equations (4) and (5) are solved using a fourth-order Runge-Kutta method.[12] To maintain precision, the velocities are scaled to 10^6 cm/s, the asymmetry frequency ω is scaled to 10^6 rad/s, and time t is scaled to 10^{-6} s. Parameters are chosen to match our typical experimental conditions: $B=364$ G, $L=76.8$ cm, $R=3.87$ cm, $a=0.178$ mm, $\phi_{\text{cw}}=-80$ V, $\phi_{10}=0.1$ V, and $n=l=1$.

III. ANALYTICAL RESULTS FOR A HELICAL ASYMMETRY IN A PERIODIC PLASMA

As a touchstone for the simulation, we present some results of an analytical treatment. We consider a plasma with periodic boundary conditions of period $2L$ and a helical asymmetry. The total potential is given by

$$\phi(r,\theta,z,t) = \phi_0(r) + \phi_1(r)\cos(kz - l\theta + \omega t), \tag{6}$$

where $\phi_0(r)$ is given by Eq. (1). In the drift approximation, we then have

$$\frac{dr}{dt} = -\frac{l\phi(r)}{rB}\sin\eta, \tag{7}$$

$$\frac{d\theta}{dt} = \frac{v_\theta}{r} = \omega_R(r) + \frac{1}{rB}\frac{d\phi_1(r)}{dr}\cos\eta, \tag{8}$$

and

$$\frac{dv_z}{dt} = -\frac{ek}{m}\phi_1(r)\sin\eta, \tag{9}$$

where $\eta=kv-l\theta+\omega t$ and $\omega_R(r)=(1/rB)(d\phi_0/dr)$ is the azimuthal $E\times B$ rotation frequency.

We first note that changes in r and v_z are simply related. From Eqs. (7) and (9) we obtain

$$\frac{rB}{l}\frac{dr}{dt} = \frac{m}{ek}\frac{dv_z}{dt}. \tag{10}$$

Integrating this between any two times, we find

$$\frac{k\omega_c}{2l}[r^2(t_2) - r^2(t_1)] = v_z(t_2) - v_z(t_1), \tag{11}$$

where $\omega_c=eB/m$ is the electron cyclotron frequency.

Next, we treat the behavior of particles trapped in the asymmetric potential. Guided by the standard treatment of particle trapping, we consider oscillations in the quantity η. Forming $d^2\eta/dt^2$ and using Eqs. (8) and (9) we obtain

$$\frac{d^2\eta}{dt^2} = \left[-\frac{ek^2}{m}\phi_1 + \frac{l^2}{rB}\phi_1\frac{d\omega_R}{dr} + \frac{l^2}{rB}\phi_1\cos\eta\frac{d}{dr}\left(\frac{1}{rB}\frac{d\phi_1}{dr}\right) + \frac{l}{rB}\frac{d\phi_1}{dr}\left(kv_z - l\frac{d\theta}{dt} - \omega\right)\right]\sin\eta. \tag{12}$$

The third term in Eq. (12) is second order in the perturbing potential ϕ_1, and thus may be ignored. The phase of the asymmetric potential will be constant in a frame moving with velocity

$$v_{\text{res}} = \frac{l\omega_R - \omega}{k}, \tag{13}$$

and in this frame the fourth term of Eq. (12) is zero to first order. We thus are left with

$$\frac{d^2\eta}{dt^2} = -\omega_T^2\sin\eta, \tag{14}$$

where

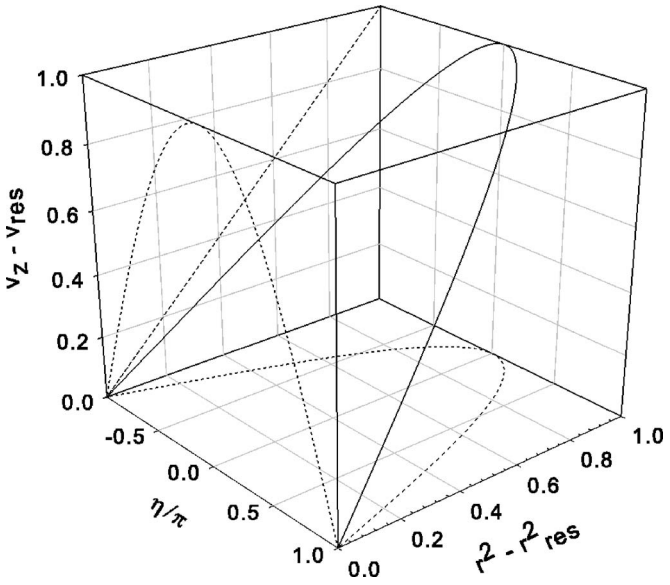

FIG. 2. Top half of the resonance island for a helical asymmetry with projections on the three backplanes. The scaling for v_z and r is given by Eqs. (16) and (11).

$$\omega_T^2 = \left(\frac{e}{m}k^2 - \frac{l^2}{rB}\frac{d\omega_R}{dr}\right)\phi_1. \tag{15}$$

Equation (14) is the well-known pendulum equation with ω_T being the small angle oscillation frequency. In this context, this is the oscillation frequency of particles moving with the asymmetry and trapped in its potential.

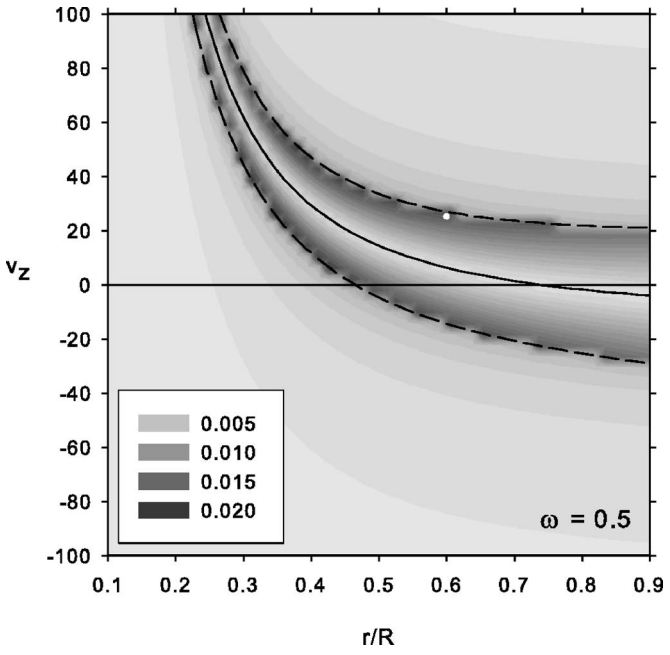

FIG. 3. Contours of scaled radial excursion $(r_{max}-r_{min})/R$ versus initial axial velocity v_z and scaled radius r/R for a helical asymmetry with periodic boundary conditions and a representative asymmetry frequency $\omega=0.5$. The solid line shows the resonant velocity v_{res} and the dotted lines the analytical boundaries of the resonance island given by Eq. (16). The white dot is the starting point for Fig. 4. Stair steps in the contours are an artifact of the square array of initial conditions.

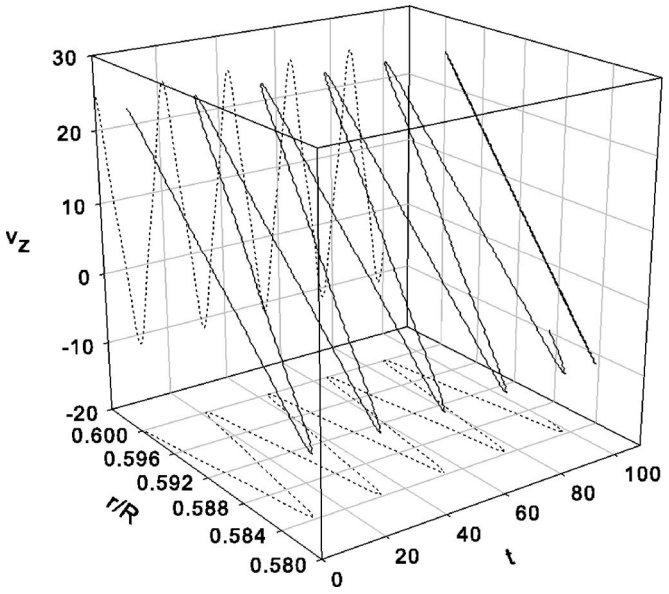

FIG. 4. Trajectory plot of v_z and r/R versus time t with projections on the three backplanes. The initial condition is $v_z=25$ and $r/R=0.6$ as shown by the white dot in Fig. 3. The regular oscillatory motion characteristic of trapped particles is consistent with expectations.

From here the analysis follows that for the standard plane wave. Oscillations in the asymmetry potential form resonance islands and these islands have half-width in the v_z- η plane of

$$\Delta v_z = 2\frac{\omega_T}{k}. \tag{16}$$

For a helical potential, the trapping oscillations also move the particle in radius, in accordance with Eq. (11). The top half of such an island is shown in Fig. 2.

IV. SIMULATION RESULTS

A. Helical asymmetry with periodic boundary conditions

We start with the simplest case of a helical asymmetry with periodic boundary conditions and show that the code produces results consistent with analytical theory. We set the initial values of r, v_z, z, and θ and run the code for a chosen asymmetry frequency ω and length of time t_{max}. Here we set the initial $z=0.05L$ and $\theta=0$ to maximize the interaction with the asymmetry and choose t_{max} to be long compared to a trapping period $2\pi/\omega_T$, where ω_T is given by Eq. (15). We run the code for a grid of 50×50 initial v_z and r values. For each initial condition, the code keeps track of the maximum and minimum values of r, v_z, and z. In Fig. 3 we show a contour plot of the scaled radial excursion $(r_{max}-r_{min})/R$ versus the initial v_z and r/R for the representative frequency $\omega=0.5$. The plot shows that certain initial conditions produce large radial excursions reflecting the resonant interaction with the asymmetry. Superimposed on the plot are lines corresponding to Eqs. (13) and (16) showing that the location and width of the resonant interaction are as expected. Particles starting just inside the resonance island have the largest radial excursions as they execute trapping oscillations. Addi-

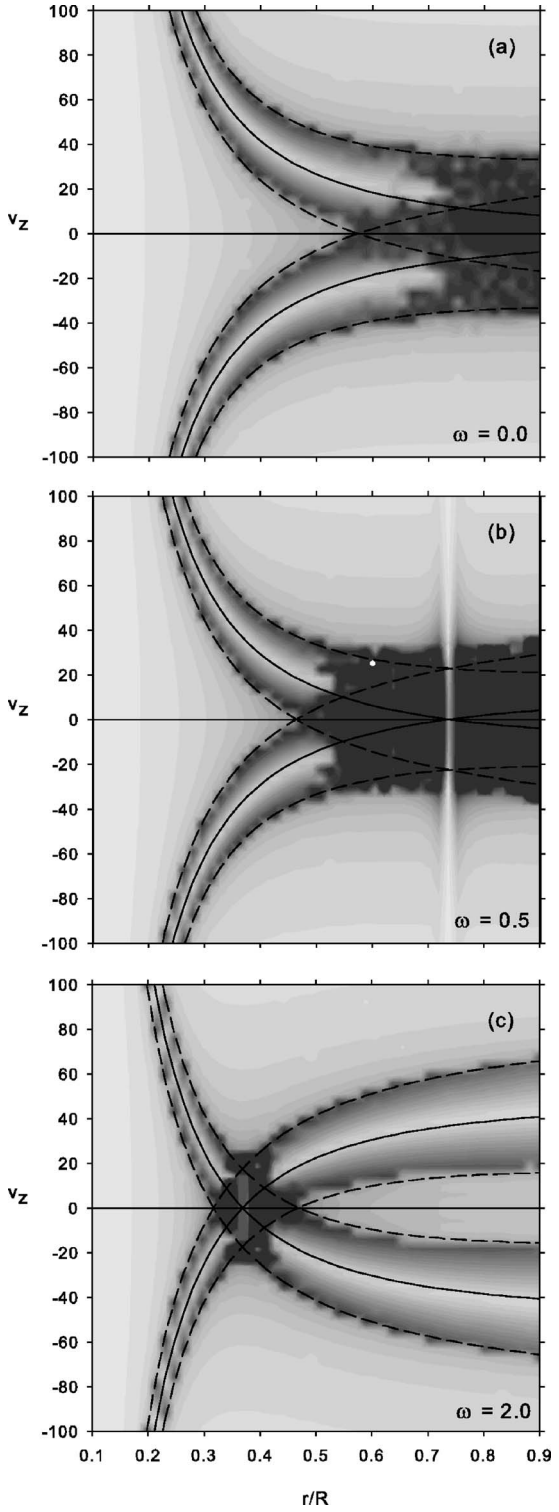

FIG. 5. Contours of scaled radial excursion versus initial axial velocity and scaled radius for a standing wave asymmetry at three representative asymmetry frequencies. The contour scale is the same as for Fig. 3. Resonant structures are seen for both of the constituent counterpropagating helical waves. When the resonances overlap, the motion becomes stochastic.

tional runs with different asymmetry frequencies show that the entire resonance structure shifts up or down according to Eqs. (13). A contour plot of the velocity excursion $v_{max}-v_{min}$ has a similar appearance due to the simple relationship given in Eq. (11).

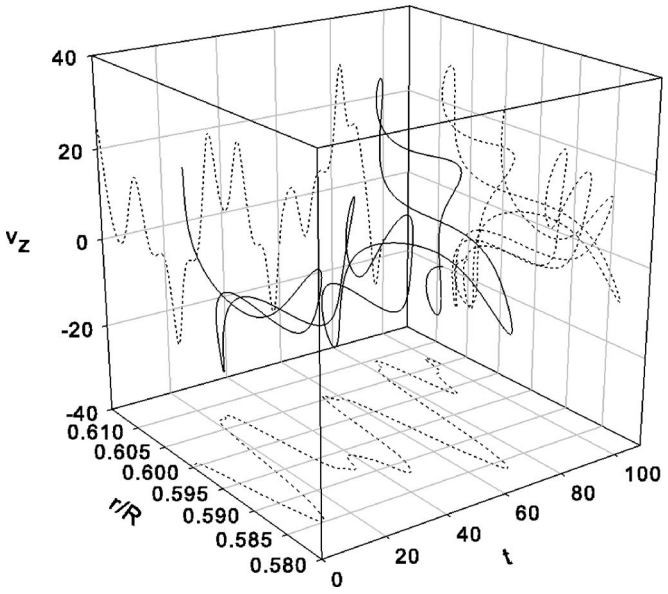

FIG. 6. Trajectory plot of v_z and r/R vs t with projections on the three backplanes. The initial condition is $v_z=25$ and $r/R=0.6$, as shown by the white dot in Fig. 5(b). The motion is no longer periodic and the relation between v_z and r no longer follows Eq. (11).

The regularity of the particle dynamics in this case is illustrated in Fig. 4. We set the initial conditions to be $v_z=25$ and $r/R=0.6$, as shown by the white dot in Fig. 3. Since this is inside the resonance island, we observe the periodic oscillations of a trapped particle. Motions in v_z and r are correlated, as expected from Eq. (11).

B. Standing wave asymmetry

We next consider the case of a standing wave asymmetry of the form of Eq. (3). For this case, the results are the same for either periodic or specularly reflecting boundary conditions. Figure 5 shows contour plots of the scaled radial excursion versus initial condition for three representative asymmetry frequencies. Since the standing wave asymmetry consists of two counterpropagating helical waves, it is no surprise to see two resonance structures with velocities of opposite sign. When the two resonances overlap, however, the regular motion of the helical asymmetry is lost. Apparently, all initial conditions in the overlap region now produce large radial excursions, not just those at the boundaries of the resonance islands.

The particle motion in the overlap regions is stochastic.[13] The regular particle dynamics for a single helical wave were characterized by periodic motion at a single frequency and correlation between v_z and r. For the standing wave, the same initial conditions produce nonperiodic, multiple frequency motion with no correlation between v_z and r, as shown in Fig. 6. Furthermore, the particle evolution exhibits sensitive dependence on initial conditions, as shown in Fig. 7.

Embedded in these stochastic regions is another type of motion. This is illustrated in Fig. 8. Part (a) shows the same data as in Fig. 5(b) with a different contour scale so that the regions of largest radial excursion are distinguished. These

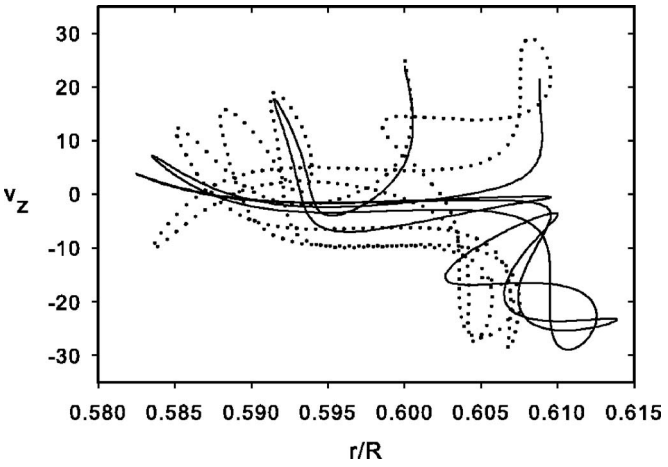

FIG. 7. Plot of v_z vs r/R for two slightly different initial conditions. The initial condition for the dotted line is $v_z=25$ and $r/R=0.6$ and is the same as shown in Fig. 6. The solid line starts at $v_z=24$ and $r/R=0.6$ but quickly diverges from the dotted line. This sensitivity to initial conditions is characteristic of stochastic motion.

appear on either side of the $v_{\mathrm{res}}=0$ point (or the $\omega=l\omega_R$ point) and are bounded in velocity by the island width. A key feature of these particles is that they are restricted to one end of the device, as shown in Fig. 8(b). This contour plot gives the axial excursion $(z_{\max}-z_{\min})$ scaled to the length L, with darker shades corresponding to shorter axial excursions. These particles are trapped in the asymmetry potential in the lab frame.

A simple model explains the features in the vicinity of $\omega=l\omega_R$. For a standing wave, we have

$$\phi_1=\phi_{10}\cos\left(\frac{n\pi}{L}z\right)\cos(-l\theta+\omega t) \tag{17}$$

and

$$E_\theta=\frac{l\phi_{10}}{r}\cos\left(\frac{n\pi}{L}z\right)\sin(-l\theta+\omega t). \tag{18}$$

It is E_θ that produces radial drift. To zeroth order, $-l\theta+\omega t=(\omega-l\omega_R)t$, so that $E_\theta=0$ at the radius where $\omega=l\omega_R$. On either side of this radius, however, there is a region where $-l\theta+\omega t$ is nonzero and is slowly varying in time. For times short compared to this variation, these particles see approximately constant fields, as represented in Fig. 9. For either reflecting or periodic boundaries, particles with low energies will be trapped axially. For these particles, $\int E_\theta dz>0$, producing large radial excursions. In contrast, untrapped particles have $\int E_\theta dz=0$.

C. Helical asymmetry with reflecting boundary conditions

Returning to the case of a helical asymmetry, we now impose reflecting boundary conditions. This change produces several new effects, as shown in Fig. 10. Although the helical asymmetry travels in one direction only, particles with both positive and negative initial velocities interact resonantly since they change directions when they reflect at the machine ends. This explains the presence of two resonance structures

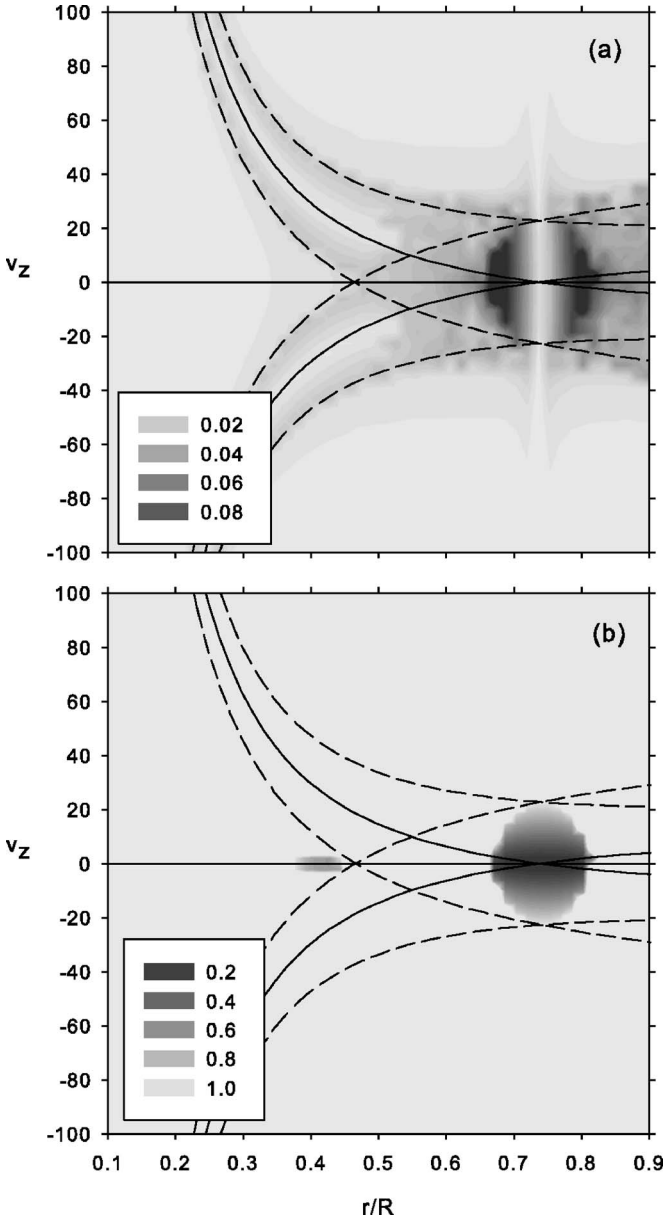

FIG. 8. (a) Replot of Fig. 5(b) with a different contour scale. Embedded in the stochastic region is a smaller region of large radial excursion around the radius where $\omega=\omega_R$. (b) Contour plot of the scaled axial excursion $(z_{\max}-z_{\min})/L$ versus initial v_z and r/R for the same conditions as (a). Note that here darker shades indicate shorter axial excursions. This shows that the region of large radial excursion has restricted axial excursion; i.e., the particles are trapped at one end of the machine.

as in the standing wave case. Note that the boundaries of the observed resonance structures lie slightly inside the lines given by Eq. (16). As in the other cases we have considered, the lines assume an asymmetry amplitude of $\phi_{10}=0.1$. The reduction in the size of the resonance structures is presumably due to the fact that the particles interact resonantly only half the time. This on-off switching of the resonant interaction may also account for the weak secondary resonance structure on the left side of Fig. 10.

The most striking feature of Fig. 10, however, is the band of large radial excursion around the radius where $\omega=l\omega_R$. Unlike the standing wave case, all velocities partici-

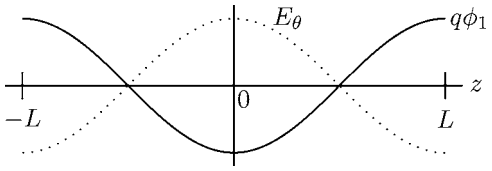

FIG. 9. Representation of standing wave fields near the point where $\omega = l\omega_R$.

pate, not just the low velocity ones. Again, a simple model explains this feature. For a helical wave, we have

$$\phi_1 = \phi_{10} \cos\left(\frac{n\pi}{L} z - l\theta + \omega t\right) \tag{19}$$

and

$$E_\theta = \frac{l\phi_{10}}{r} \sin\left(\frac{n\pi}{L} z - l\theta + \omega t\right). \tag{20}$$

If $\omega = \omega_R$, then $(-l\theta + \omega t) = 0$, so these particles see constant fields as represented in Fig. 11. Note that, for periodic boundaries ($z = -L$ to L), in first order, $\int E_\theta dz = 0$, whether the particles are axially trapped or not. However, for reflecting boundaries (0 to L), $\int E_\theta dz > 0$, whether the particles are axially trapped or not. Thus, all velocities near this radius undergo large radial excursions.

D. Realistic ends

Finally, we consider the effect of realistic end conditions on the simulation results. The particles still reflect at the ends of the machine, but the reflection point is now a function of radius and particle energy, and the length of the axial excursion will no longer be the same as the asymmetry axial wavelength. In addition, the rotation frequency ω_R will have an additional contribution due to the radial component of the confining end fields, thus making ω_R a function of z as well as r.

One might conclude that all these changes would destroy the resonant interaction we have previously observed, but this is not the case. For gate potentials matching those in our experiment (−140 V), contour plots such as Fig. 5 show two very small changes. The first is that the position of the resonance structure is altered such that, for a given radius, its center occurs at a slightly smaller velocity. This is consistent with a slight decrease in the effective length of the plasma (i.e., the particle axial excursion). This decrease produces a decrease in v_{res} in accordance with Eq. (13).

The second change is the appearance of a weak secondary resonance similar to that seen in Fig. 10. This is due to the fact that the plasma length is no longer the same as the asymmetry wavelength. The particle thus sees an asymmetry that is not a pure sine wave and the higher k values in this asymmetry produce the secondary resonance structure.

V. DISCUSSION

These results show that there are dynamical behaviors that are not included in the current theory of asymmetry-induced transport.[10] While this work does not constitute a new transport theory, the results appear to point in a promising direction. Furthermore, while the details of the results shown reflect our experimental configuration (most notably, the radial dependence of ω_R), the new dynamical behaviors do not depend on these particulars and should also be present in other experiments.

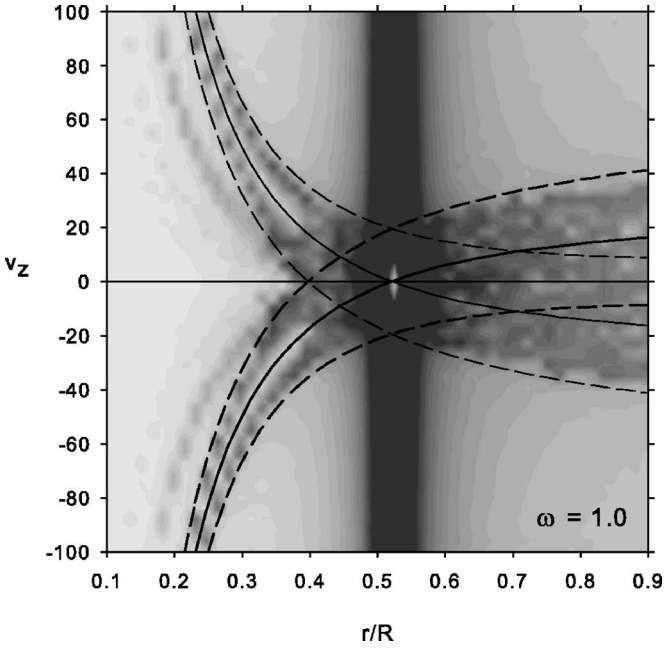

FIG. 10. Contours of scaled radial excursion versus initial axial velocity and scaled radius for a helical asymmetry with reflecting boundary conditions and a representative asymmetry frequency $\omega = 1.0$. The contour scale is the same as for Fig. 3.

The most experimentally relevant case is that of a standing wave asymmetry since the wall probe signals applied in most experiments can be analyzed into one or more standing waves. When the asymmetry frequency ω matches $l\omega_R$ at some radius in the plasma, the particle dynamics will be stochastic. In the canonical studies of stochasticity due to resonance overlap, there is a transition point when the amplitude of the two resonances becomes large enough to produce the overlap.[13] Here, however, overlap always occurs because the resonances cross through one another. Although the width of the stochastic region in velocity space depends on the amplitude of the asymmetry, there is no transition to stochasticity at a particular asymmetry amplitude.

We have also noted the presence of a region of especially large radial excursion around the $\omega = l\omega_R$ point. These particles are also trapped axially by the asymmetry potential. For an $n = 1$, $l = 1$ asymmetry like the one used here, there

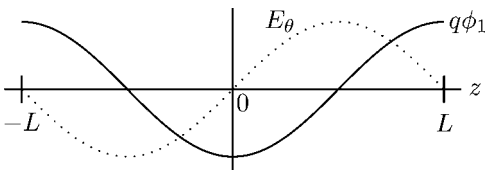

FIG. 11. Representation of helical fields near the point where $\omega = l\omega_R$.

would be a trapped particle population at each end of the machine separated by 180° in θ. This is reminiscent of recent work on trapped particle modes.[14]

Note that both of these effects involve the lowest velocity particles. If heating of the plasma occurs, this population of particles would be reduced. This may explain why the "rotating wall" technique requires some form of cooling to be effective.[3,8] The observed "no-slip" requirement (i.e., $\omega \approx l\omega_R$) of these experiments is also consistent with our simulation results.

Our results also suggest that there may be fundamental differences between experiments that use a static asymmetry (i.e., $\omega=0$) and those that use a nonzero frequency. Since ω_R stays positive out to the wall of the device, a static asymmetry will not produce resonances that cross. While a region of resonance overlap may occur for this case [cf. Fig. 5(a)], it will occur at the larger radii and, since the resonances do not cross, may exhibit a transition to stochasticity. The same comments apply to asymmetries that are made to spin in the direction opposite the plasma (i.e., asymmetries with $\omega<0$). Such considerations might also explain why our experiments with variable frequency asymmetries[7] observe significant transport only for nonzero, positive frequencies.

Finally, we note that for the helical case with reflecting boundaries large radial excursions occur around the $\omega=l\omega_R$ point for all velocities, so that heating would not reduce this population. This suggests that a helical rotating wall could produce improved confinement without the need for supplemental cooling of the plasma.

VI. CONCLUSION

We have studied the particle dynamics of asymmetry-induced transport using a single-particle computer simulation. For the case of a helical asymmetry with periodic boundary conditions we observe behaviors consistent with analytical theory. For reflecting boundaries with either a helical or standing wave asymmetry, we observe important dynamical behaviors not included in the current theory of this transport.

ACKNOWLEDGMENTS

This material is based upon work supported by the Department of Energy under award number DE-FG02-06ER54882. The author acknowledges seminal contributions to this work by Calvin Liang and Jason Dexter.

[1] D. L. Eggleston, T. M. O'Neil, and J. H. Malmberg, Phys. Rev. Lett. **53**, 982 (1984).
[2] J. Notte and J. Fajans, Phys. Plasmas **1**, 1123 (1994).
[3] X.-P. Huang, F. Anderegg, E. M. Hollman, C. F. Driscoll, and T. M. O'Neil, Phys. Rev. Lett. **78**, 875 (1997).
[4] J. M. Kriesel and C. F. Driscoll, Phys. Rev. Lett. **85**, 2510 (2000).
[5] D. L. Eggleston and B. Carrillo, Phys. Plasmas **9**, 786 (2002).
[6] E. Gilson and J. Fajans, Phys. Rev. Lett. **90**, 015001 (2003).
[7] D. L. Eggleston and B. Carrillo, Phys. Plasmas **10**, 1308 (2003).
[8] J. R. Danielson and C. M. Surko, Phys. Plasmas **13**, 055706 (2006).
[9] Y. Soga, Y. Kiwamoto, and N. Hashizume, Phys. Plasmas **13**, 052105 (2006).
[10] D. L. Eggleston and T. M. O'Neil, Phys. Plasmas **6**, 2699 (1999).
[11] Y. Kiwamoto, Y. Soga, and J. Aoki, Phys. Plasmas **12**, 094501 (2005).
[12] R. Hornbeck, *Numerical Methods* (Quantum, New York, 1975), pp. 194–196.
[13] A. J. Lichtenberg and M. A. Lieberman, *Regular and Stochastic Motion* (Springer-Verlag, New York, 1983), pp. 213–258.
[14] A. A. Kabantsev and C. F. Driscoll, Phys. Rev. Lett. **89**, 245001 (2002).